nature communications

Article

https://doi.org/10.1038/s41467-024-53140-5

Creating and controlling global Greenberger-Horne-Zeilinger entanglement on quantum processors

Received: 1 April 2024

Accepted: 30 September 2024

Published online: 12 October 2024

Check for updates

Zehang Bao[1,5], Shibo Xu[1,5], Zixuan Song[1], Ke Wang[1], Liang Xiang[1], Zitian Zhu[1], Jiachen Chen[1], Feitong Jin[1], Xuhao Zhu[1], Yu Gao[1], Yaozu Wu[1], Chuanyu Zhang[1], Ning Wang[1], Yiren Zou[1], Ziqi Tan[1], Aosai Zhang[1], Zhengyi Cui[1], Fanhao Shen[1], Jiarun Zhong[1], Tingting Li[1], Jinfeng Deng[1], Xu Zhang[1], Hang Dong[1], Pengfei Zhang[1], Yang-Ren Liu[2], Liangtian Zhao[3], Jie Hao[3], Hekang Li[1], Zhen Wang[1,4], Chao Song[1], Qiujiang Guo[1,4] ✉, Biao Huang[2] ✉ & H. Wang[1,4] ✉

Greenberger-Horne-Zeilinger (GHZ) states, also known as two-component Schrödinger cats, play vital roles in the foundation of quantum physics and the potential quantum applications. Enlargement in size and coherent control of GHZ states are both crucial for harnessing entanglement in advanced computational tasks with practical advantages, which unfortunately pose tremendous challenges as GHZ states are vulnerable to noise. Here we propose a general strategy for creating, preserving, and manipulating large-scale GHZ entanglement, and demonstrate a series of experiments underlined by high-fidelity digital quantum circuits. For initialization, we employ a scalable protocol to create genuinely entangled GHZ states with up to 60 qubits, almost doubling the previous size record. For protection, we take a different perspective on discrete time crystals (DTCs), originally for exploring exotic nonequilibrium quantum matters, and embed a GHZ state into the eigenstates of a tailor-made cat scar DTC to extend its lifetime. For manipulation, we switch the DTC eigenstates with in-situ quantum gates to modify the effectiveness of the GHZ protection. Our findings establish a viable path towards coherent operations on large-scale entanglement, and further highlight superconducting processors as a promising platform to explore nonequilibrium quantum matters and emerging applications.

The ability to generate, preserve, and manipulate highly entangled quantum states is a long-term goal for building practical quantum computers that can outperform classical machines[1–3]. Among various multipartite entangled states, GHZ states[4] constitute a peculiar class showing the strongest nonlocal entanglement for N particles[5]. On the other hand, they are the most fragile entangled states[6,7]. External perturbations on any single particle can destroy the entanglement, and thermalization can arise internally through many-body dynamics if

[1]School of Physics, ZJU-Hangzhou Global Scientific and Technological Innovation Center, and Zhejiang Key Laboratory of Micro-nano Quantum Chips and Quantum Control, Zhejiang University, Hangzhou, China. [2]Kavli Institute for Theoretical Sciences, University of Chinese Academy of Sciences, Beijing, China. [3]Institute of Automation, Chinese Academy of Sciences, Beijing, China. [4]Hefei National Laboratory, Hefei, China. [5]These authors contributed equally: Zehang Bao, Shibo Xu. ✉e-mail: qguo@zju.edu.cn; phys.huang.biao@gmail.com; hhwang@zju.edu.cn

interactions exist[8]. Therefore, creating high-quality GHZ states with larger size and higher fidelity is a standard benchmark for showing the performance of quantum hardware[9–12]. Although multipartite entanglement of tens of particles has been created across different physical platforms[9–17], the generation of maximally entangled GHZ states, achieving state fidelity of $\mathcal{F} > 0.5$ which can verify N-particle entanglement, has so far been limited to $N \approx 30$[9,12,15,16,18]. Heading towards the more challenging realm of preserving and manipulating such fragile states, a fully-fledged experiment is still pending[7].

Preserving GHZ states using a discrete time crystal (DTC) is an uncharted territory. Previously, DTC has attracted broad scientific interest as an exotic nonequilibrium matter[19–22], which extends the fundamental concept of spontaneous symmetry breaking to time translations[23,24]. Ergodicity-breaking mechanisms of many-body localization (MBL)[25–27] and prethermalization[28,29] have been employed to induce time-crystalline dynamics of product states across a wide range of physical platforms[30–39]. DTCs are also considered as potential candidates to accommodate GHZ states by their robust cat eigenstate pairs[19,40,41]. However, this intriguing application has never been achieved. MBL DTC could generate numerous cat eigenstates, but the presence of disorders may lead to unpredictable instability[42–44]. Meanwhile, prethermal DTC is disorder-free, but the strong diffusion restricts cats eigenstates to be spatially homogeneous ones[20,35,45,46]. By contrast, the third venue[19] of weak ergodicity breaking[47–50] by a cat scar DTC, where a few Fock-space localized cat eigenstates (cat scars) are deterministically engineered to define a subspace with time-crystalline ordering that is analytically tractable[51], has come to the fore as a potential solution.

In this article, we report a series of experiments evidencing the possibility of creating, preserving, and manipulating GHZ entanglement on superconducting quantum processors. We first generate up to 60-qubit GHZ states with fidelities $\mathcal{F}$ all far above 0.5, unambiguously verifying genuine global entanglement. Creating this large entanglement is enabled by the high fidelity of around 0.999 and 0.995 for single- and two-qubit gates, respectively, and an efficient entangling scheme along radial path scalable in two dimensions (2D). We further digitally implement the cat scar DTC with thousands of quantum gates to protect the created GHZ state and manipulate its dynamics. To quantify the protection of DTC, we develop a quantum sensing protocol and observe a subharmonic temporal response for the macroscopic coherent phase of the GHZ state. Remarkably, the phase oscillation is observed throughout 30 cycles under generic perturbation, indicating a DTC lifetime longer than those under non-interacting Rabi drivings and under free decay. The oscillation amplitudes are unaffected even if we further manipulate both the GHZ state and cat scars during evolution, accomplishing a smooth in situ switch of protection between different GHZ states.

Results

Generating GHZ state

We first demonstrate the generation of N-qubit GHZ states

$$|\Phi, \boldsymbol{s}\rangle_N = \left(|\boldsymbol{s}\rangle + e^{-i\Phi}|\bar{\boldsymbol{s}}\rangle\right)/\sqrt{2}, \tag{1}$$

where $|\boldsymbol{s}\rangle$ is an N-bit Fock basis, with each bit encoding a qubit in either ground (0) or excited (1) state, and $|\bar{\boldsymbol{s}}\rangle$ is that with all bits of $|\boldsymbol{s}\rangle$ flipped. In this experiment, we choose $|\boldsymbol{s}\rangle$ to be of antiferromagnetic ordering, i.e., $|0101\ldots\rangle$. The phase factor Φ quantifies the coherence between Fock bases $|\boldsymbol{s}\rangle$ and $|\bar{\boldsymbol{s}}\rangle$.

To create $|\Phi, \boldsymbol{s}\rangle_N$ among qubits in 2D, we design an efficient protocol based on a set of unitaries including $X(\pi)$, Hadamard, and CNOT gates (see "Methods" and Supplementary Note 2). As illustrated in Fig. 1a, after a layer of single-qubit gates, this protocol starts with a CNOT on two qubits around the center of the qubit layout, and then radially entangles peripherals stepwise by appending layers of CNOTs. In the realization, we compile the set of unitaries in Fig. 1a into a digital quantum circuit composed of experimentally accessible single-qubit rotational and two-qubit controlled π-phase gates, whose combined effect is denoted with a unitary U_{GHZ}. Running similar digital quantum circuits, we can entangle up to 60 qubits on Processor I and achieve genuine multipartite entanglement with $\mathcal{F} = 0.595 \pm 0.008$ for $N = 60$ (Fig. 1b). We emphasize that our protocol is universal as it can be adapted to any particular qubit layout topology in 2D. In a parallel effort, we entangle all 6×6 qubits on Processor II[52] with

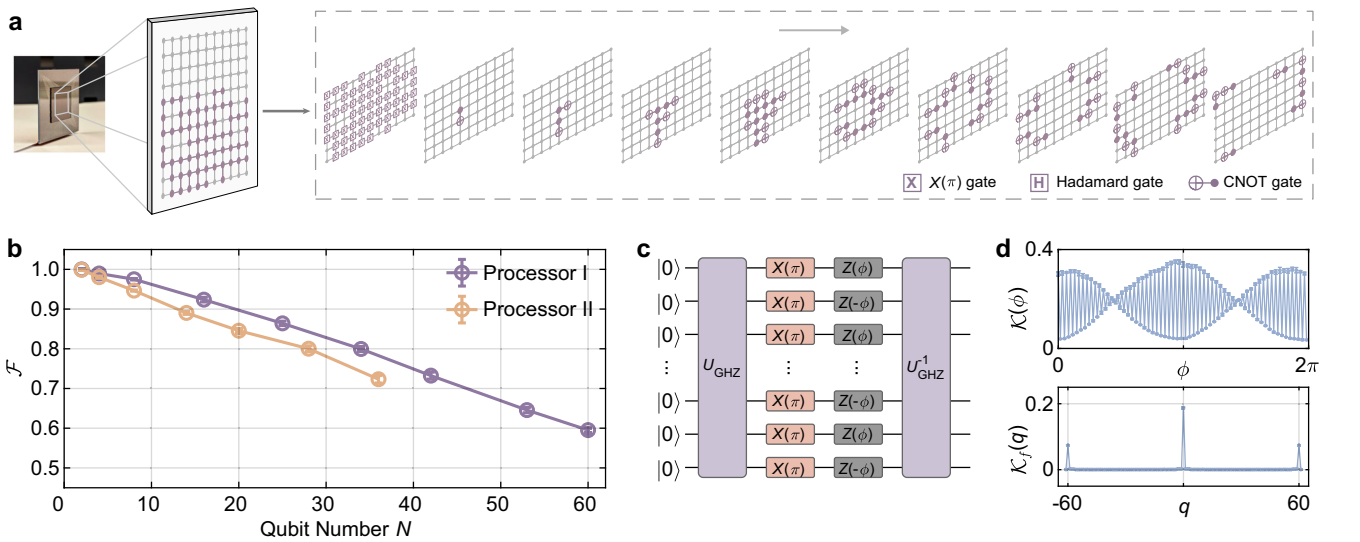

Fig. 1 | Generation and characterization of GHZ states. a Illustration of the superconducting quantum processor I and that of a general entangling protocol based on a set of quantum gates, the latter of which is further compiled into experimentally accessible elementary gates to generate the 60-qubit GHZ state. **b** Measured GHZ state fidelity $\mathcal{F}$ as functions of qubit number N for Processors I and II. The higher $\mathcal{F}$ for Processor I is likely due to its slightly better single-qubit gates. **c** MQC circuit diagram based on $Z(\pm\phi)$ and reversal of U_{GHZ}. $X(\pi)$ is a spin-echo pulse for preserving the qubit coherence, and virtual $Z(\phi)$ [$Z(-\phi)$] is applied to individual qubits in 0 (1) as recorded in basis $|\boldsymbol{s}\rangle$. **d** Measured $\mathcal{K}(\phi)$ for the 60-qubit GHZ state and its Fourier spectrum $\mathcal{K}_f(q)$. Slow sinusoidal envelope results from sparse sampling[58], which does not affect our analysis. Error bars in all figures throughout the text, if shown, are obtained by repeated measurements. See Supplementary Note 3 for more details.

$\mathcal{F} = 0.723 \pm 0.010$ for $N = 36$. Numerical simulations suggest that the reported $\mathcal{F}$ values are consistent with our calibrated gate fidelities (see "Methods" and Supplementary Note 3.C).

We attempt to measure major elements of the GHZ density matrix to obtain $\mathcal{F}$. Two diagonal elements $P_{\boldsymbol{s}}$ and $P_{\bar{\boldsymbol{s}}}$, the probabilities of finding the qubits in Fock bases $|\boldsymbol{s}\rangle$ and $|\bar{\boldsymbol{s}}\rangle$ respectively, can be directly probed. Several methods, such as measuring parity oscillation[12,15,53] and sliced Wigner function[54] can be used to probe off-diagonal elements, but here we resort to the more scalable multiple quantum coherence (MQC) protocol[55–58]. With the MQC circuit shown in Fig. 1c, the appropriate phase gates $Z(\pm\phi)$ (see "Methods") on individual qubits imprint an enhanced phase of $N\phi$, resulting in $|-(\Phi+N\phi),\boldsymbol{s}\rangle_N$. Subsequent reversal of $U_{\rm GHZ}$, referred to as $U_{\rm GHZ}^{-1}$, disentangles these N qubits and steers them back to ground state $|0000\ldots\rangle$ with a probability $\mathcal{K}(\phi)$, which displays fast sinusoidal oscillations at a rate $\propto N$. Figure 1d exemplifies such measured $\mathcal{K}(\phi)$ signal for $N = 60$ qubits and the corresponding Fourier amplitude, in which the Fourier peak $\mathcal{K}_f(q = N)$ characterizes the off-diagonal elements. As such, GHZ state fidelity is given by $\mathcal{F} = (P_{\boldsymbol{s}} + P_{\bar{\boldsymbol{s}}})/2 + \sqrt{\mathcal{K}_f(N)}$[58] (Fig. 1b). We emphasize that the MQC protocol tends to underestimate $\mathcal{F}$ since the detection is not instantaneous but involves a long sequence of gates in $U_{\rm GHZ}^{-1}$ (see Supplementary Note 3).

Cat scar DTC

For a GHZ state defined in Eq. (1), where $|\boldsymbol{s}\rangle$ can be more generic than the antiferromagnetic pattern with alternating 0 and 1, we are able to design and realize a cat scar DTC model that naturally accommodates the entanglement. Here and below, we focus on Processor II with 36 qubits for proof-of-principle experiments. As illustrated in Fig. 2a, we construct a perturbed Ising chain ($N = 36$) of periodic boundary on Processor II. Under the periodic driving, the Floquet unitary $U_{\rm F} = U_2 U_1$ per cycle is given by

$$U_1 = \left(\prod_{j=1}^{N} e^{-i\varphi_1\sigma_j^z/2} e^{i\lambda_1\sigma_j^y/2} e^{-i\varphi_2\sigma_j^z/2}\right) e^{-i\pi\sum_{j=1}^{N}\sigma_j^x/2}$$
$$U_2 = e^{-i\sum_{j=1}^{N} J_j \tilde{\sigma}_j^z(\lambda_2)\tilde{\sigma}_{j+1}^z(\lambda_2)}, \tag{2}$$

where $\sigma_j^{x,y,z}$ are Pauli matrices on Q_j, φ_1 and φ_2 are introduced to break the integrability of the model while avoiding fine-tuned echoes, and λ_1 is the single-qubit perturbing strength. U_2 characterizes the perturbed Ising interaction with $\tilde{\sigma}_j^z(\lambda_2) = \cos(\lambda_2)\sigma_j^z + \sin(\lambda_2)\sigma_j^x$. The strong Ising interaction $|J_j| = J$, comparable with Floquet driving frequency $1/T$, and the qubit-flip pulses $e^{-i\pi\sum_{j=1}^{N}\sigma_j^x/2}$ are essential ingredients.

In the unperturbed limit $\lambda_1, \lambda_2 = 0$, Ising interaction structures all eigenstates to be degenerate doublets $|\boldsymbol{s}\rangle, |\bar{\boldsymbol{s}}\rangle$, while spin-flip pulses further combine them into cat eigenstates. In particular, there are two pairs of cat eigenstates isolated from all the others by large quasienergy or qubit pattern differences, such that they, as cat scars, remain robust when all perturbations are turned on[51], as illustrated in Fig. 2b. Here, the inverse participation ratio for a Floquet eigenstate $|\epsilon_m\rangle$, i.e., $U_{\rm F}|\epsilon_m\rangle = e^{i\epsilon_m}|\epsilon_m\rangle$, reads $\mathrm{IPR}(\epsilon_m) = \sum_{\boldsymbol{s}} |\langle\epsilon_m|\boldsymbol{s}\rangle|^4$. A larger value of IPR indicates stronger Fock space localization and, therefore, better quality of a cat eigenstate to store and protect a GHZ state. It is seen

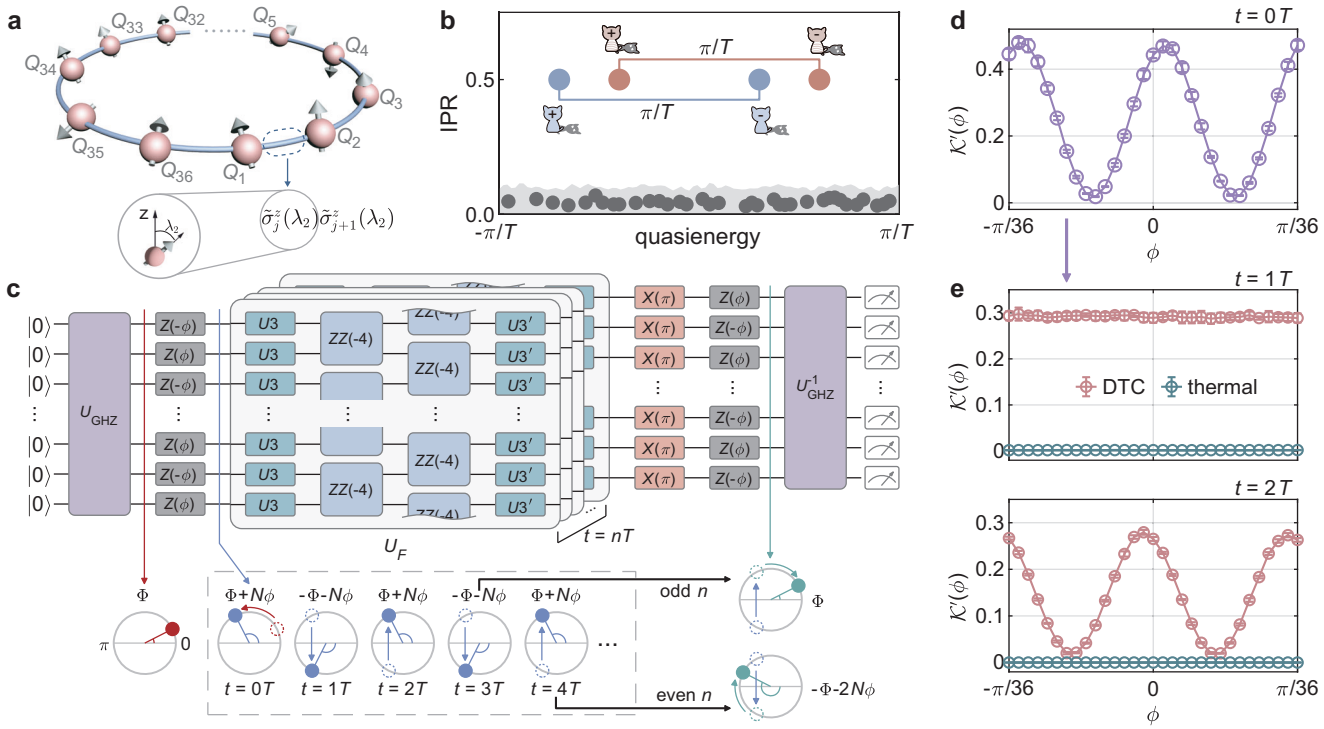

Fig. 2 | Cat scar DTC and Schrödinger cat interferometry. a Schematic representation of the 36-qubit Ising chain. Neighboring qubits are coupled by a perturbed Ising interaction. **b** Eigenstructure of a cat scar DTC. With strong Ising interaction, $|J_j| = J \sim 1/T \gg |\lambda_1|, |\lambda_2|$, two pairs of cat scars $(|\Phi, \boldsymbol{s}\rangle_N$ with $\boldsymbol{s} = 0101\ldots$ and $0000\ldots$, shown as blue and red dots, respectively, with IPR → 0.5) remain localized in Fock space under generic perturbations, in contrast to the majority thermal eigenstates (gray dots with IPR → 0). Two cat scars within each pair are separated by a quasienergy gap π/T. **c** Schrödinger cat interferometry. The circuit is similar to the MQC protocol in Fig. 1c but with an extra layer of reversed-phase rotations to detect the phase oscillations of a GHZ state. In the DTC unitary $U_{\rm F}$, $U3$ is the single-qubit rotation with 3 Euler angles and $ZZ(-4) = \exp(-i\sigma_j^z\sigma_{j+1}^z)$ (see Supplementary Note 4 for more details). Lower panel: Evolution of a GHZ state viewed on the xy plane with the poles defined by $|\boldsymbol{s}\rangle$ and $|\bar{\boldsymbol{s}}\rangle$. The initial GHZ state picks up a phase due to $Z(\pm\phi)$ and becomes $|\Phi + N\phi, \boldsymbol{s}\rangle_N$. Under DTC evolutions inside the gray dashed box, phase oscillation occurs as the GHZ state alternates between $|\pm(\Phi + N\phi), \boldsymbol{s}\rangle_N$. Afterward, the echo and reversed phase rotation double (or cancel) the coherent phase $N\phi$ for even (or odd) driving cycles. $U_{\rm GHZ}^{-1}$ disentangles the qubits and $\mathcal{K}'(\phi, t)$ in Eq. (3) is measured by the ground state probability. **d**, **e** Exemplary measurements of $\mathcal{K}'(\phi, t)$ at three consecutive instants for an initial GHZ state evolved by DTC (red circles) or thermal unitaries (green circles).

that two pairs of cat scars (IPR → 0.5) stand out, based on which we experimentally choose the homogeneous case $J_j = +1$ so that one of the two pairs naturally accommodates the generated GHZ state.

We implement U_F in the DTC regime with perturbations $\lambda_1 = \lambda_2 = 0.05$ and strong detuning from echoes $\varphi_1 = -\pi/2$, $\varphi_2 = \pi/2 - 0.6$. This is realized by a digital quantum circuit (Fig. 2c). To quantify a dynamical GHZ state, we design a quantum sensing protocol dubbed Schrödinger cat interferometry. As shown in Fig. 2c, only an extra layer of reversal phase rotation $Z(\pm\phi)$ is introduced here, such that the scalability of the MQC protocol is fully inherited. The ground state probability measured at the end of the circuit in Fig. 2c corresponds to the physical quantity

$$\mathcal{K}'(\phi, t) = \left| \left\langle -(\Phi + N\phi), \boldsymbol{s} \right| U_F^{t/T} \left| \Phi + N\phi, \boldsymbol{s} \right\rangle \right|^2. \quad (3)$$

GHZ state oscillations $U_F^{t/T}|\Phi + N\phi, \boldsymbol{s}\rangle \sim |(-1)^{t/T}(\Phi + N\phi), \boldsymbol{s}\rangle$ are then sharply revealed by the alternation of $\mathcal{K}'(\phi,t)$ between constructive $\sim \cos(2N\phi + \Phi)$ and total destructive ~1 interference for ϕ-dependence at consecutive driving periods. As exemplified in Fig. 2d, for an initial GHZ state ($N = 36$), the measured $\mathcal{K}'(\phi, t = 0)$ exhibits an evident period-$\pi/36$ oscillation (Fig. 2d). Under the DTC dynamics, the oscillation vanishes at odd period $t = 1T$ (the upper panel in Fig. 2e) and reappears in the subsequent even period $t = 2T$ (the lower panel in Fig. 2e). In contrast, a thermal system modeled by large perturbations ($\lambda_1 = 0.3$, $\lambda_2 = 0.4$) quickly erases the initial global entanglement, leaving a vanishing $\mathcal{K}'(\phi,t)$ (Fig. 2e) (see "Methods" and Supplementary Note 5.D).

Preserving GHZ state

To illustrate the long-time dynamics and benchmark the protective effects of DTC, we perform Fourier transformation of $\mathcal{K}'(\phi,t)$ on ϕ for t from 0 to $30T$, where the Fourier peak $\mathcal{K}'_f(q = 2N, t)$ exhibits a period-$2T$ oscillation of DTC orders (Fig. 3), corresponding to the pattern alternations as shown in Fig. 2e. In comparison, we perform a parallel measurement for $\mathcal{K}'_f(2N,t)$ in a non-interacting Rabi model, which amounts to replacing the two-qubit gates of the DTC with the same length of idle delay while keeping all single-qubit Rabi drivings intact, i.e., $U_F = U_1$ in Eq. (2). Thus, the real-time of each cycle remains consistent with $T = 144$ ns for both cases. A qualitative difference emerges in Fig. 3. In DTC, $\mathcal{K}'_f(2N,t)$ is chiefly damped by external noise effects, leading to an exponential decay ~e^{-t}. In contrast, the Rabi driving case suffers from an additional term $\sim e^{-t^2}$ due to the fact that $\lambda_1 \neq 0$, which signals the delocalization of a GHZ state from the original Fock bases. This apparent difference in Fig. 3 indicates that the cat scar DTC integrates both dynamical decoupling of Rabi drivings[59] and strong Ising interactions, achieving improved protection on GHZ states. Note for the free-decay case without any protection, i.e., keeping all qubits idle without any circuits, its quantum coherence loses approximately three times more quickly than that in DTC (Supplementary Note 5).

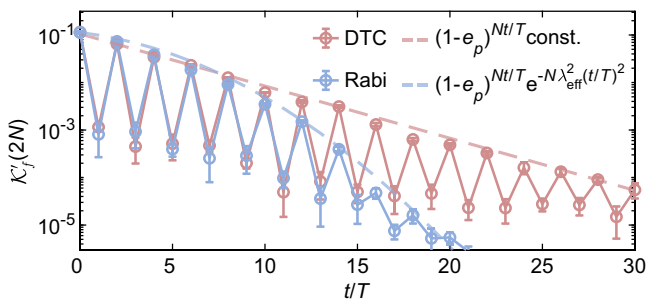

Fig. 3 | GHZ dynamics preserved in cat scar DTC. Measured $\mathcal{K}'_f(2N,t)$ dynamics in DTC (red circles) and the benchmark against that under non-interacting Rabi drivings (blue circles). Dashed lines are analytical results. Here, the constant in legend is $\sqrt{2} \cdot \sqrt{\text{IPR}} \approx 0.92$ with the IPR of cat scar given by analytical perturbation theory, while for the Rabi driving case $\lambda_{\text{eff}} \approx 0.0239$, the coefficient parametrizing the combined effect of all perturbative factors, can be rigorously obtained (see Supplementary Note 5). The effective cycle error per qubit is estimated based on an apparent match between the analytical results and experimental data, which yields $e_p = 0.007$ in DTC and $e_p = 0.003$ for the Rabi driving case.

We note that the sensitive GHZ state offers long-sought opportunities to directly reveal the spectral-paired cat eigenstates, a defining property of long-range-entangled DTCs[26,51,60]. We show in Supplementary Note 5 that disentangling each qubit in the eigenstate reduces the value of $\mathcal{K}'_f$ exponentially, in contrast to a vanishing impact to conventional probes, like magnetic orders for product states. Thus, $\mathcal{K}'_f$ in Fig. 3 opens the door to accurately seeing genuine N-body entanglement in individual eigenstates.

Manipulating GHZ dynamics

In previous experiments, we have fixed the antiferromagnetic qubit pattern in a GHZ state and focused on the dynamics of coherent phase Φ. Practically, it is desirable to switch the scarred subspace such that it becomes compatible with a generic GHZ state, even better if the switch takes place seamlessly during evolution. To identify the method of editing scarred subspace, we first note that thermalization in a cat scar DTC occurs in a structured way. Specifically, under strong and uniform Ising interaction $J_j = 1$, a spin can only be flipped by perturbations if it is sandwiched by *anti-parallel* neighbors, i.e., 011 ↔ 001, because such a process conserves the Ising energy. Contrarily, antiferromagnetic patterns (i.e., 0101…) are immune to perturbations, while global antiferromagnetic states constitute scarred subspace. Such a constraint is revealed by the site-resolved detection of the connected correlation function

$$G_{jk}(t) = \left| \left\langle \sigma_j^z(t) \sigma_k^z(t) \right\rangle - \left\langle \sigma_j^z(t) \right\rangle \left\langle \sigma_k^z(t) \right\rangle \right|, \quad (4)$$

where $\sigma_j^z(t) = (U_F^{t/T})^\dagger \sigma_j^z U_F^{t/T}$. It approaches 1 for a perfect GHZ state, while $G_{jk}(t) \to 0$ if the Q_j-Q_k pair is disentangled. In Fig. 4a and b, we initialize a 36-qubit GHZ state $|\Phi, \boldsymbol{s}\rangle_N$ and flip Q_{19} immediately, so that the 5-qubit chain in $\boldsymbol{s}$, $Q_{17}Q_{18}Q_{19}Q_{20}Q_{21}$, changes from "01010" to "01110". Then, thermalization is ignited at Q_{18} and Q_{20} according to the kinetic constraint, as we see in Fig. 4a, a cross-shaped thermal region centering around Q_{19} occurs for $G_{jk}(t = 24T)$. Taking an average $G_j(t) = (1/35)\sum_{k \neq j} G_{jk}(t)$, we observe a light-cone $|j - 19| = v_B t$ propagating from Q_{18} and Q_{20} in Fig. 4b, with the analytical $v_B \approx 0.038$ approximately obtained under the kinetic constraint condition. The fact that thermalization occurs locally strongly indicates that a local dressing can also hinder such a process.

We exemplify the modification of cat-scarred subspace in a new $\tilde{U}_F$, where we locally reverse the sign of Ising interaction at $J_{18} = J_{19} = -1$ while keeping all other $J_j = +1$ unchanged. Such a sign reversal is experimentally realized by inserting a pair of $X(\pi)$ gates on the flipped Q_{19}, which are located around the $ZZ(-4)$ gate of the original U_F sequence, as illustrated in Fig. 4c. Then, the kinetic constraint is modified locally for Q_{18} and Q_{20}, so that each of them is only vulnerable to perturbative flips if it is sandwiched by *parallel* neighbors. Contrarily, processes like "011" ↔ "001" for spin chain $Q_{17}Q_{18}Q_{19}$ now violate the conservation of local Ising energy, i.e., $-J_{17} + J_{18} = -2 \neq +J_{17} - J_{18} = +2$, with $J_{17} = -J_{18} = 1$, and therefore cannot occur. Thus, the source of thermalization in Fig. 4a and b is extinguished, and the new GHZ state, $|\Phi, \boldsymbol{s}\rangle_N$ with Q_{19}, flipped, now resides inside the new scarred subspace. Correspondingly, we recover $G_{jk}(t)$ in Fig. 4d for the previous cross-shaped thermal region.

To demonstrate dynamical switching and benchmark the efficiency of editing scarred subspace with $X(\pi)$ gates, we consider the GHZ state with pattern $\boldsymbol{s}' = 00110011\ldots$, which is obtained by generating $|\Phi, \boldsymbol{s}\rangle_N$ and then flipping qubits with the indices $j = 4m + 2\,\&\,4$

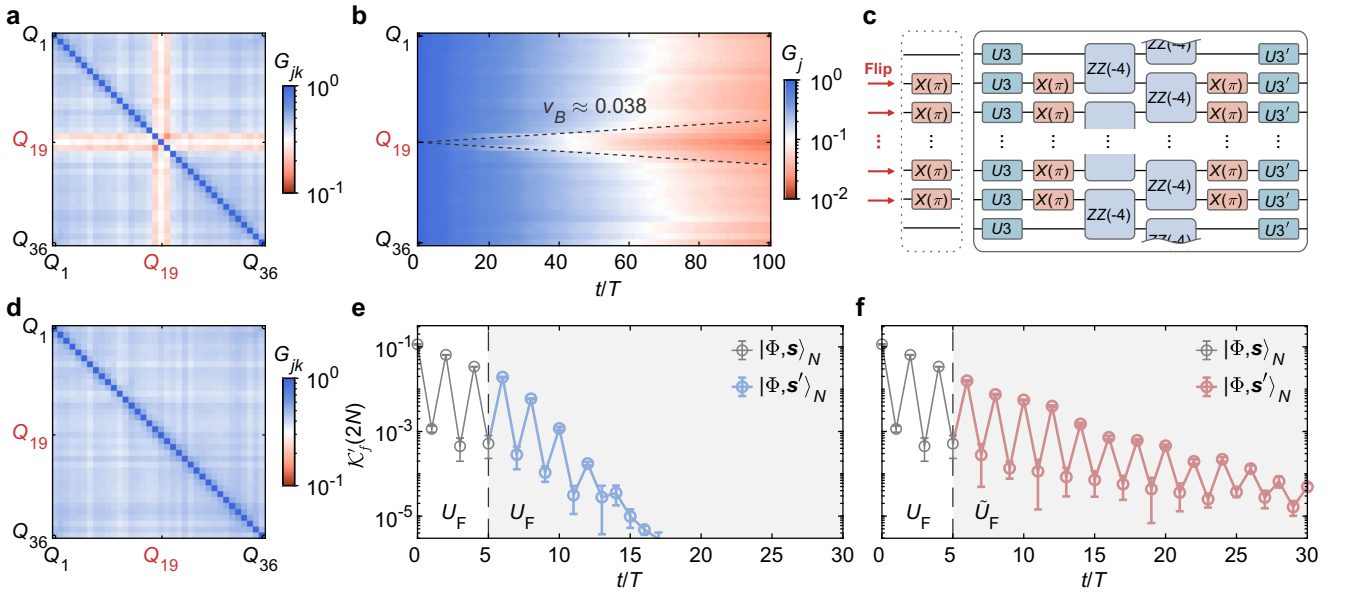

Fig. 4 | Manipulating cat scar DTC to protect the switched GHZ states. a $G_{jk}(t)$ measured, e.g., at $t = 24T$ under the evolution of U_F for a 36-qubit GHZ state, which is created by flipping Q_{19} of $|\Phi,\boldsymbol{s}\rangle_N$ at $t = 0$. **b** Measured $G_j(t)$ dynamics for the same initial GHZ state as in (**a**), where a light cone emerges around the flipped site Q_{19}. Dashed lines are the analytical predictions of the thermalizing light cone with the mean butterfly velocity $v_B \approx 0.038$ (see Supplementary Note 5). **c** Exemplary quantum circuit diagram of $\tilde{U}_F$, which illustrates a scheme to edit the original U_F for effectively reversing the sign of local Ising interaction with $X(\pi)$ gates. The exact circuit layout of $\tilde{U}_F$ depends on the spin pattern of the generic GHZ state, which is produced by the left-most layer of $X(\pi)$ flip gates acting on $|\Phi,\boldsymbol{s}\rangle$. **d** $G_{jk}(t)$ measured at $t = 24T$ under the evolution of a compatible $\tilde{U}_F$ for the same initial GHZ state as in (**a**). In (**a**, **b**, and **d**), experimental results are sample-averaged, including 10 random φ_1 to exclude the effects of possible single-qubit echoes, and for each φ_1 the flipped spin is sampled over six physical qubits to reduce the detrimental effect of the qubit non-uniformity. **e** Measured $\mathcal{K}'_f(2N)$ dynamics under the evolution of the original U_F. The GHZ state is switched from the initial $|\Phi,\boldsymbol{s}\rangle_N$ to $|\Phi,\boldsymbol{s}'\rangle_N$ by flipping 18 qubits at $t = 5T$. **f** Measured $\mathcal{K}'_f(2N)$ dynamics for conditions similar to those in (**e**), except that the DTC unitary is switched from U_F to a compatible $\tilde{U}_F$ at $t = 5T$. The cat scar DTC timely catches up with spin flips, so that protection is kept effective at longer times compared with that in (**e**).

$m+3$, for $m = 0, 1, \ldots, N/4-1$. Such a generic GHZ state thermalizes most rapidly under the original U_F with $J_j = +1$, because every single qubit is a source for thermalization. A compatible $\tilde{U}_F$ involves $N/2$ pairs of $X(\pi)$ gates, with one pair for each flipped qubit. We start with the 36-qubit GHZ state, $|\Phi,\boldsymbol{s}\rangle_N$, which oscillates in a compatible cat scar DTC (U_F) for 5 cycles as in Fig. 3. Then, we flip appropriate qubits to produce $|\Phi,\boldsymbol{s}'\rangle_N$, and continue the evolution under two conditions: The GHZ state is evolved in the original U_F, verifying a rapid decay after the switch (Fig. 4e); in contrast, the phase oscillation persists resulting from a simultaneous switching from U_F to the new $\tilde{U}_F$ (Fig. 4f), witnessing a similar amplitude as in Fig. 3a.

Discussion

Here, a set of concepts and protocols to preserve, control, and detect macroscopic quantum coherence in nonequilibrium many-body dynamics is developed, opening a new avenue for exploring large-scale GHZ states and practical applications of nonequilibrium quantum matters[19,34]. We not only create a 60-qubit GHZ state with genuine global entanglement but also push the research front toward preserving its coherence and controlling its dynamics. Meanwhile, for the studies of DTC, our findings offer the long-sought-after direct evidence of spectral-paired cat eigenstates, which establishes a new perspective of using nonequilibrium eigenstructures to steer unconventional quantum dynamics.

In a broader spectrum, our findings bridge central topics in quantum computation with those in the emergent nonequilibrium quantum many-body physics[19]. A tantalizing direction is to engineer the eigenstate structure of a wider range of exotic nonequilibrium matters as control knobs to steer multipartite entanglement[48]. In addition to DTC, long-range entangled eigenstates also exist in Floquet spin liquids[61,62], dynamical scars in fracton matters[63], and string-net models[64], based on which, further development of our platform to larger size and higher fidelity, provides an ideal testbed to design new frameworks for versatile applications[65,66] in quantum information, quantum metrology, and error correction.

Methods

Experimental Setup

Our experiments are carried out on two superconducting processors featuring transmon qubits arranged on a square lattice, one with 60 qubits selected (Processor I in Fig. 1a) and the other one with 36 qubits (Processor II). Each qubit can be individually excited by microwave pulse for rotation of its state around an arbitrary axis in the xy plane of the Bloch sphere, e.g., x-axis by an angle θ, noted as $X(\theta)$; phase gate $Z(\theta)$ is virtually applied by recording the phase θ in subsequent microwaves. Single-qubit rotation with 3 Euler angles, referred to as $U3(\alpha, \beta, \theta)$ in the main text, is effectively a rotation gate plus a virtual $Z(\theta)$. Any two neighboring qubits have a tunable coupler, so that controlled ϕ-phase gates can be dynamically implemented, which are used to assemble controlled π-phase gates for creating GHZ states and the two-qubit ZZ interaction required in cat scar DTC. For both processors, all physical single- and two-qubit gates are calibrated to be of high precision, with average gate fidelity around 0.999 and 0.995, respectively. As such, we are able to observe relevant experimental features even by executing digital quantum circuits with more than 300 layers in depth, which consist of about 7000 quantum gates (see Supplementary Notes 1 and 2 for more details).

Data availability

The data generated in this study have been deposited in the Zenodo database under the accession code https://doi.org/10.5281/zenodo.13785116[67].

Code availability

We utilized the quantum platform MindSpore Quantum[68] to perform numerical simulations for the quantum circuits in our experiments. The simulation codes used in this study are available on GitHub at https://github.com/ZJU-zbao/ghz-60q.

References

1. Amico, L., Fazio, R., Osterloh, A. & Vedral, V. Entanglement in many-body systems. *Rev. Mod. Phys.* **80**, 517–576 (2008).
2. Horodecki, R., Horodecki, P., Horodecki, M. & Horodecki, K. Quantum entanglement. *Rev. Mod. Phys.* **81**, 865–942 (2009).
3. Nielsen, M. A. & Chuang, I. L.*Quantum Computation and Quantum Information: 10th Anniversary Edition* (Cambridge University Press, 2011).
4. Greenberger, D. M., Horne, M. A., Shimony, A. & Zeilinger, A. Bell's theorem without inequalities. *Am. J. Phys.* **58**, 1131–1143 (1990).
5. Gisin, N. & Bechmann-Pasquinucci, H. Bell inequality, bell states and maximally entangled states for n qubits. *Phys. Lett. A* **246**, 1–6 (1998).
6. Pezzè, L., Smerzi, A., Oberthaler, M. K., Schmied, R. & Treutlein, P. Quantum metrology with nonclassical states of atomic ensembles. *Rev. Mod. Phys.* **90**, 035005 (2018).
7. Fröwis, F., Sekatski, P., Dür, W., Gisin, N. & Sangouard, N. Macroscopic quantum states: Measures, fragility, and implementations. *Rev. Mod. Phys.* **90**, 025004 (2018).
8. Abanin, D. A., Altman, E., Bloch, I. & Serbyn, M. Colloquium: Many-body localization, thermalization, and entanglement. *Rev. Mod. Phys.* **91**, 021001 (2019).
9. Moses, S. A. et al. A race-track trapped-ion quantum processor. *Phys. Rev. X* **13**, 041052 (2023).
10. Graham, T. M. et al. Multi-qubit entanglement and algorithms on a neutral-atom quantum computer. *Nature* **604**, 457–462 (2022).
11. Bluvstein, D. et al. Logical quantum processor based on reconfigurable atom arrays. *Nature* **626**, 58–65 (2024).
12. Omran, A. et al. Generation and manipulation of Schrödinger cat states in Rydberg atom arrays. *Science* **365**, 570–574 (2019).
13. Cao, S. et al. Generation of genuine entanglement up to 51 superconducting qubits. *Nature* **619**, 738–742 (2023).
14. Pogorelov, I. et al. Compact ion-trap quantum computing demonstrator. *PRX Quantum* **2**, 020343 (2021).
15. Song, C. et al. Generation of multicomponent atomic Schrödinger cat states of up to 20 qubits. *Science* **365**, 574–577 (2019).
16. Wang, X.-L. et al. 18-Qubit entanglement with six photons' three degrees of freedom. *Phys. Rev. Lett.* **120**, 260502 (2018).
17. Xu, S. et al. Digital simulation of projective non-abelian anyons with 68 superconducting qubits. *Chin. Phys. Lett.* **40**, 060301 (2023).
18. Mooney, G. J., White, G. A. L., Hill, C. D. & Hollenberg, L. C. L. Generation and verification of 27-qubit Greenberger-Horne-Zeilinger states in a superconducting quantum computer. *J. Phys. Commun.* **5**, 095004 (2021).
19. Zaletel, M. P. et al. Colloquium: Quantum and classical discrete time crystals. *Rev. Mod. Phys.* **95**, 031001 (2023).
20. Khemani, V., Moessner, R. & Sondhi, S. L. A Brief History of Time Crystals. Preprint at https://doi.org/10.48550/arXiv.1910.10745 (2019).
21. Else, D. V., Monroe, C., Nayak, C. & Yao, N. Y. Discrete time crystals. *Annu. Rev. Condens. Matter Phys.* **11**, 467–499 (2020).
22. Sacha, K. & Zakrzewski, J. Time crystals: a review. *Rep. Progr. Phys.* **81**, 016401 (2017).
23. Wilczek, F. Quantum time crystals. *Phys. Rev. Lett.* **109**, 160401 (2012).
24. Wilczek, F. Superfluidity and space-time translation symmetry breaking. *Phys. Rev. Lett.* **111**, 250402 (2013).
25. Khemani, V., Lazarides, A., Moessner, R. & Sondhi, S. L. Phase structure of driven quantum systems. *Phys. Rev. Lett.* **116**, 250401 (2016).
26. Else, D. V., Bauer, B. & Nayak, C. Floquet time crystals. *Phys. Rev. Lett.* **117**, 090402 (2016).
27. Yao, N. Y., Potter, A. C., Potirniche, I.-D. & Vishwanath, A. Discrete time crystals: Rigidity, criticality, and realizations. *Phys. Rev. Lett.* **118**, 030401 (2017).
28. Else, D. V., Bauer, B. & Nayak, C. Prethermal phases of matter protected by time-translation symmetry. *Phys. Rev. X* **7**, 011026 (2017).
29. Machado, F., Else, D. V., Kahanamoku-Meyer, G. D., Nayak, C. & Yao, N. Y. Long-range prethermal phases of nonequilibrium matter. *Phys. Rev. X* **10**, 011043 (2020).
30. Randall, J. et al. Many-body–localized discrete time crystal with a programmable spin-based quantum simulator. *Science* **374**, 1474–1478 (2021).
31. Frey, P. & Rachel, S. Realization of a discrete time crystal on 57 qubits of a quantum computer. *Sci. Adv.* **8**, eabm7652 (2022).
32. Mi, X. et al. Time-crystalline eigenstate order on a quantum processor. *Nature* **601**, 531–536 (2022).
33. Zhang, J. et al. Observation of a discrete time crystal. *Nature* **543**, 217–220 (2017).
34. Choi, S. et al. Observation of discrete time-crystalline order in a disordered dipolar many-body system. *Nature* **543**, 221–225 (2017).
35. Kyprianidis, A. et al. Observation of a prethermal discrete time crystal. *Science* **372**, 1192–1196 (2021).
36. Beatrez, W. et al. Critical prethermal discrete time crystal created by two-frequency driving. *Nat. Phys.* **19**, 407–413 (2023).
37. Stasiuk, A. & Cappellaro, P. Observation of a prethermal *U*(1) discrete time crystal. *Phys. Rev. X* **13**, 041016 (2023).
38. Kongkhambut, P. et al. Observation of a continuous time crystal. *Science* **377**, 670–673 (2022).
39. Zhang, X. et al. Digital quantum simulation of Floquet symmetry-protected topological phases. *Nature* **607**, 468–473 (2022).
40. Choi, S., Yao, N. Y. & Lukin, M. D. Quantum metrology based on strongly correlated matter. Preprint at https://doi.org/10.48550/arXiv.1801.00042 (2017).
41. Kozin, V. K. & Kyriienko, O. Quantum time crystals from hamiltonians with long-range interactions. *Phys. Rev. Lett.* **123**, 210602 (2019).
42. Sels, D. Bath-induced delocalization in interacting disordered spin chains. *Phys. Rev. B* **106**, l020202 (2022).
43. Morningstar, A., Colmenarez, L., Khemani, V., Luitz, D. J. & Huse, D. A. Avalanches and many-body resonances in many-body localized systems. *Phys. Rev. B* **105**, 174205 (2022).
44. Léonard, J. et al. Probing the onset of quantum avalanches in a many-body localized system. *Nat. Phys.* **19**, 481–485 (2023).
45. Luitz, D. J., Moessner, R., Sondhi, S. L. & Khemani, V. Prethermalization without temperature. *Phys. Rev. X* **10**, 021046 (2020).
46. Ippoliti, M., Kechedzhi, K., Moessner, R., Sondhi, S. & Khemani, V. Many-body physics in the NISQ Era: Quantum programming a discrete time crystal. *PRX Quantum* **2**, 030346 (2021).
47. Turner, C. J., Michailidis, A. A., Abanin, D. A., Serbyn, M. & Papić, Z. Weak ergodicity breaking from quantum many-body scars. *Nat. Phys.* **14**, 745–749 (2018).
48. Maskara, N. et al. Discrete time-crystalline order enabled by quantum many-body scars: Entanglement steering via periodic driving. *Phys. Rev. Lett.* **127**, 090602 (2021).
49. Bernien, H. et al. Probing many-body dynamics on a 51-atom quantum simulator. *Nature* **551**, 579–584 (2017).
50. Bluvstein, D. et al. Controlling quantum many-body dynamics in driven rydberg atom arrays. *Science* **371**, 1355–1359 (2021).

51. Huang, B. Analytical theory of cat scars with discrete time-crystalline dynamics in Floquet systems. *Phys. Rev. B* **108**, 104309 (2023).
52. Yao, Y. et al. Observation of many-body Fock space dynamics in two dimensions. *Nat. Phys.* **19**, 1459–1465 (2023).
53. Sackett, C. A. et al. Experimental entanglement of four particles. *Nature* **404**, 256–259 (2000).
54. Rundle, R. P., Mills, P. W., Tilma, T., Samson, J. H. & Everitt, M. J. Simple procedure for phase-space measurement and entanglement validation. *Phys. Rev. A* **96**, 022117 (2017).
55. Baum, J., Munowitz, M., Garroway, A. N. & Pines, A. Multiple-quantum dynamics in solid state NMR. *J. Chem. Phys.* **83**, 2015–2025 (1985).
56. Gärttner, M. et al. Measuring out-of-time-order correlations and multiple quantum spectra in a trapped-ion quantum magnet. *Nat. Phys.* **13**, 781–786 (2017).
57. Doronin, S. I. Multiple quantum spin dynamics of entanglement. *Phys. Rev. A* **68**, 052306 (2003).
58. Wei, K. X. et al. Verifying multipartite entangled Greenberger-Horne-Zeilinger states via multiple quantum coherences. *Phys. Rev. A* **101**, 032343 (2020).
59. Suter, D. & Álvarez, G. A. Colloquium: Protecting quantum information against environmental noise. *Rev. Mod. Phys.* **88**, 041001 (2016).
60. von Keyserlingk, C. W., Khemani, V. & Sondhi, S. L. Absolute stability and spatiotemporal long-range order in Floquet systems. *Phys. Rev. B* **94**, 085112 (2016).
61. Sun, B.-Y., Goldman, N., Aidelsburger, M. & Bukov, M. Engineering and probing non-abelian chiral spin liquids using periodically driven ultracold atoms. *PRX Quantum* **4**, 020329 (2023).
62. Kalinowski, M., Maskara, N. & Lukin, M. D. Non-abelian floquet spin liquids in a digital rydberg simulator. *Phys. Rev. X* **13**, 031008 (2023).
63. Pai, S. & Pretko, M. Dynamical scar states in driven fracton systems. *Phys. Rev. Lett.* **123**, 136401 (2019).
64. Liu, Y.-J., Shtengel, K., Smith, A. & Pollmann, F. Methods for simulating string-net states and anyons on a digital quantum computer. *PRX Quantum* **3**, 040315 (2022).
65. Iemini, F., Fazio, R. & Sanpera, A. Floquet time crystals as quantum sensors of ac fields. *Phys. Rev. A* **109**, L050203 (2024).
66. Yousefjani, R., Sacha, K. & Bayat, A. Discrete time crystal phase as a resource for quantum enhanced sensing. Preprint at https://doi.org/10.48550/arXiv.2405.00328 (2024).
67. Bao, Z. ZJU-zbao/ghz-60q-data: Creating and controlling global Greenberger-Horne-Zeilinger entanglement on quantum processors (v1.0). https://doi.org/10.5281/zenodo.13785116 (2024).
68. MindQuantum Developer. MindQuantum, version 0.9.11. https://gitee.com/mindspore/mindquantum (2021).

Acknowledgements

We thank Rubem Mondaini, Dong-Ling Deng for the helpful discussion, and Siwei Tan for technical support. The device was fabricated at the Micro-Nano Fabrication Center of Zhejiang University. Numerical simulation of quantum circuits was performed using the MindSpore Quantum framework. We acknowledge support from the National Natural Science Foundation of China (Grant Nos. 92065204, 12274368, 12174389, U20A2076, 12174342, 12274367, and 12322414), the Innovation Program for Quantum Science and Technology (Grant No. 2021ZD0300200), the National Key Research and Development Program of China (Grant No. 2023YFB4502600), and the Zhejiang Provincial Natural Science Foundation of China (Grants No. LR24A040002 and LDQ23A040001). Q.G. is also supported by the Zhejiang Pioneer (Jianbing) Project (Grant No. 2023C01036). H.W. is also supported by the New Cornerstone Science Foundation through the XPLORER PRIZE.

Author contributions

B.H. and Q.G. conceived the idea; Z.B. and S.X. carried out the experiments and analyzed the experimental data under the supervision of Q.G., C.S., and H.W.; B.H. and Y.L. conducted the theoretical analysis; H.L. and J.C. fabricated the device supervised by H.W.; Q.G., B.H., Z.B., and H.W. co-wrote the manuscript; H.W., Q.G., C.S., Z.W., Z.B., S.X., Z.S., K.W., L.X., Z.Z., J.C., F.J., X.Z., Y.G., Y.W., C.Z., N.W., Y.Z., Z.T., A.Z., Z.C., F.S., J.Z., T.L., J.D., X.Z., H.D., P.Z., L.Z., and J.H. contributed to experimental setup; All authors contributed to the discussions of the results and the writing of the manuscript.

Competing interests

The authors declare no competing interests.

Additional information

Supplementary information The online version contains supplementary material available at https://doi.org/10.1038/s41467-024-53140-5.

Correspondence and requests for materials should be addressed to Qiujiang Guo, Biao Huang or H. Wang.

Peer review information *Nature Communications* thanks the anonymous reviewers for their contribution to the peer review of this work. A peer review file is available.